Thermal-, Pressure-, and Light-Induced Spin Transition in Novel Cyanide-Bridged Fe^{II}–Ag^{I} Bimetallic Compounds with Three-Dimensional Interpenetrating Double Structures $\{Fe^{II}L_x[Ag(CN)_2]_2\}\cdot G$

Virginie Niel,[a] M. Carmen Muñoz,[b] Ana B. Gaspar,[a] Ana Galet,[a] Georg Levchenko,[c] and José Antonio Real*[a]

Abstract: Low-spin, high-spin and spin-transition behaviours have been observed for the doubly interpenetrating three-dimensional bimetallic compounds $\{Fe^{II}(pz)[Ag(CN)_2]_2\}.pz$ (pz = pyrazine), $\{Fe^{II}(4,4'\text{-bipy})_2[Ag(CN)_2]_2\}$ (4,4′-bipy = 4,4′-bipyridine), and $\{Fe^{II}(bpe)_2[Ag(CN)_2]_2\}$ (bpe = bispyridylethylene), respectively. The single crystals of the bpe derivative undergo a spin transition with a large hysteresis loop at about 95 K. After several warming and cooling cycles, the single crystals become a microcrystalline powder with 50% spin transition. Influence of pressure- as well as light-induced excited spin-state trapping (LIESST) on the thermal 50% spin transition of the microcrystalline sample has also been investigated. Thermal spin-transition behaviour has also been induced at pressures higher than 1 bar for the 4,4′-bipy derivative. Both the 4,4′-bipy and bpe derivatives show strong pressure dependence of the spin state at 300 K.

Keywords: cooperative phenomena · cyanides · interpenetrating 3D structures · iron · spin crossover

Introduction

The search for novel bistable molecular compounds is of critical importance for developing new functional materials like sensors and memory devices. In this regard, iron(II) spin-crossover compounds represent one of the best examples of molecular bistability.[1] For these compounds the energy gap between the fundamental low-spin (LS) state and the excited high-spin (HS) state is close to the thermal energy, hence, a spin-state conversion can be driven by a variation of temperature or pressure and by light irradiation.[2] The LS ↔ HS conversion is concomitant with a variation of the iron-to-ligand bond length, which is around 0.2 Å greater for the HS state.[3] This change of molecular size is transmitted cooperatively from one site to another in the crystal through intermolecular interactions, that hydrogen bonding, π-stacking and by suitable bridging ligands. For strong intersite coupling, thermal hysteresis and, consequently, bistability can be observed for these systems.

In the course of the studies involving the design and synthesis of new Hofmann-like clathrate compounds, Kitazawa et al. synthesised and characterised the 2D spin-crossover compound $\{Fe(py)_2[Ni(CN)_4]\}$ (py = pyridine).[4] This compound undergoes a cooperative spin transition between 210 and 170 K with a hysteresis loop about 6 K wide. In a recent paper we reported the synthesis and characterisation of the $[M(CN)_4]^{2-}$ (M = Pd, Pt) derivatives of the $\{Fe(py)_2[M(CN)_4]\}$ system.[5] Both derivatives display similar spin conversion with critical temperatures in the range 208–216 K. Furthermore, this 2D spin-crossover system seemed to us a good opportunity to study the changes that may occur in cooperativity when dimensionality changes from 2D to 3D, by slightly modifying the axial ligand, for instance, by replacing py by pyrazine (pz). The resulting 3D system of formula $\{Fe(pz)[M(CN)_4]\}\cdot 2H_2O$ (M = Ni, Pd, Pt) showed a remarkable increase of the width of the hysteresis loop from 7 K to 33 K, as well as a shift of the critical temperatures towards room temperature.[5]

Following the systematic investigation of the chemistry of the Hofmann-like clathrates undertaken since 1970s by Iwamoto and co-workers,[6] we decided to explore the possibilities of other cyanide complexes like $[M^{I}(CN)_2]^-$ (M = Cu, Ag, Au) in the field of the spin-crossover phenomenon. In this paper we report the synthesis, crystal structure and magnetic and photomagnetic properties of new bimetallic

[a] Prof. Dr. J. A. Real, V. Niel, A. B. Gaspar, A. Galet
Departament de Química Inorgánica
Institut de Ciencia Molecular, Universitat de València
Dr. Moliner 50, 46100 Burjassot, València (Spain)
Fax: (+34) 96-386-43-22
E-mail: jose.a.real@uv.es

[b] Prof. Dr. M. C. Muñoz
Departament de Física Aplicada
Universitat Politècnica de València
Camino de Vera s/n, 46071 València (Spain)

[c] Prof. Dr. G. Levchenko
Donetsk Physical-Technical Institute
National Academy of Science of Ukraine
R. Luxemburg Strasse 72, Donetsk, 83114 (Ukraine)

  0947-6539/02/0811-2446 $ 20.00+.50/0

doubly interpenetrated 3D complexes of formula $\{Fe(L)_x[Ag(CN)_2]_2\}\cdot G$, in which L = pz, $x = 1$, G = pz (**1**); L = 4,4′-bipy, $x = 2$ (**2**) and L = bp, $x = 2$ (**3**). A variety of magnetic behaviours has been observed: **1** is LS, **2** is HS, and **3** undergoes a very cooperative spin transition with a 95 K-wide hysteresis loop. In addition, the effect of pressure on the thermal variation of the magnetic susceptibility has been investigated for **2** and **3**.

Results

Crystal Structure of 1, 2 and 3: Figure 1 shows a perspective drawing of compounds **1**–**3**, together with the atom numbering scheme. Selected crystallographic data and bond lengths and angles are listed in Tables 1 and 2, respectively. The crystal structures of **1**, **2** and **3** are closely related to that previously reported by Iwamoto et al. for $\{Cd(4,4'\text{-bipy})_2[Ag(CN)_2]_2\}$.[6c] They are made up of two interpenetrating 3D networks consisting of parallel stacks of 2D $\{Fe[Ag(CN)_2]_2\}$ sheets running along the [001] (**1**) or [101] (**2**, **3**) direction. The organic ligands pz, 4,4′-bipy and bpe thread the meshes of the immediately adjacent $\{[Ag(CN)_2]_2\}_n$ networks and bridge iron–iron (**1**) and iron–silver (**2**, **3**) atom pairs of subsequent networks.

Table 1. Crystallographic Data for **1**, **2** and **3**.

formula	$C_{12}H_8Ag_2Fe_1N_8$	$C_{24}H_{16}Ag_2Fe_1N_8$	$C_{28}H_{20}Ag_2Fe_1N_8$
M_w	535.85	688.04	740.11
space group	*Cmcm* (63)	$P2_1/n$ (14)	$P2_1/n$ (14)
a [Å]	12.815(5)	8.656(2)	9.5175(15)
b [Å]	15.979(3)	11.625(3)	11.380(2)
c [Å]	6.7705(11)	12.769(4)	13.2043(15)
β [°]		103.61(2)	95.180(12)
V [Å^3]	1386.4(7)	1248.7(6)	1424.4(4)
Z	4	2	2
T [K]	293(2)	293(2)	293(2)
λ [Å]	0.71073	0.71073	0.71073
μ [mm^{-1}]	3.840	2.155	1.896
ρ_{calc} [g cm^{-3}]	2.567	1.830	1.726
$R1$	0.0928	0.0224	0.0484
$wR2$	0.2478	0.0596	0.1025

$R1 = \Sigma||F_o| - |F_c||/\Sigma|F_o|$; $wR2 = [\Sigma[w(F_o^2 - F_c^2)^2/\Sigma[w(F_o^2)^2]]^{1/2}$. $w = 1/[\sigma^2(F_o^2) + (mP)^2 + nP]$ in which $P = (F_o^2 + 2F_c^2)/3$ (m = 0.1471 (**1**), 0.0467 (**2**) or 0.0489 (**3**); n = 118.4614 (**1**), 2.6918 (**2**) or 0 (**3**)).

Table 2. Selected bond lengths [Å] and angles [°] for **1**, **2** and **3**.

	(1)	(2)	(3)
Fe–N(1)	1.91(3)	2.129(3)	2.129(7)
Fe–N(2)	1.99(3)	2.188(3)	2.172(9)
Fe–N(3)	1.98(2)	2.248(3)	2.232(7)
Ag–C(1)	2.08(4)	2.109(4)	2.102(8)
Ag–C(2)	2.04(3)	2.107(4)	2.079(9)
Ag–N(4)[a]		2.466(3)	
Ag–N(4)[b]			2.508(8)
N(1)–C(1)	1.16(4)	1.136(5)	1.134(10)
N(2)–C(2)	1.12(4)	1.141(5)	1.148(11)
N(1)-Fe-N(2)	90.6(11)	87.73(12)	87.0(3)
N(1)-Fe-N(2)[c]	179.8(11)		
N(1)-Fe-N(2)[d]		92.27(12)	
N(1)-Fe-N(2)[e]			93.0(3)
N(2)-Fe-N(3)	89.6(5)	89.80(12)	89.2(3)
N(1)-Fe-N(3)	90.4(6)	91.97(12)	90.9(3)
C(1)-Ag-C(2)	176.2(17)	154.24(14)	157.4(3)
N(4)[a]-Ag-C(1)		99.62(13)	
N(4)[b]-Ag-C(1)			97.6(3)
N(4)[a]-Ag-C(2)		105.49(13)	
N(4)[b]-Ag-C(2)			103.9(3)

The atoms marked with a letter are generated with the following symmetry operations: a : $1-x, y, 1-z$; b : $-x-1/2, y+1/2, -z+1/2$; c: $1-x, y, 1/2-z$; d: $-x, 2-y, 2-z$; e: $1-x, 1-y, 1-z$.

The silver atoms, in the $[Ag(CN)_2]^-$ units of **1**, display an almost linear coordination [C(1)-Ag-C(2) = 177.5(2)°] with bond lengths Ag–C = 2.05(3) Å. In contrast, they are three-coordinate in **2** and **3**; consequently, the C(1)-Ag-C(2) moieties are bent [C(1)-Ag-C(2) = 159.24(1)° (**2**) and 157.4(3)° (**3**)]. The Ag–C(1), Ag–C(2), and Ag–N(4)[1] bond lengths are 2.107(4) Å (**2**) / 2.102(8) Å (**3**), 2.109(4) Å (**2**) / 2.079(9) Å (**3**) and 2.466(3) Å [$i = x-1, y, z-1$] (**2**) / 2.508(9) Å [$i = -x-1/2, y, -z+1/2$] (**3**), respectively.

The terminal N(1) and N(2) atoms of the $[Ag(CN)_2]^-$ groups fill the basal coordination positions lying in the x,y plane (**1**) and in the plane parallel to [010] direction (**2**, **3**) of the $[FeN_6]$ pseudooctahedral site. In the case of **1**, a binary C_2 axis passing through the iron atom bisects the N(1)-Fe-N(2)

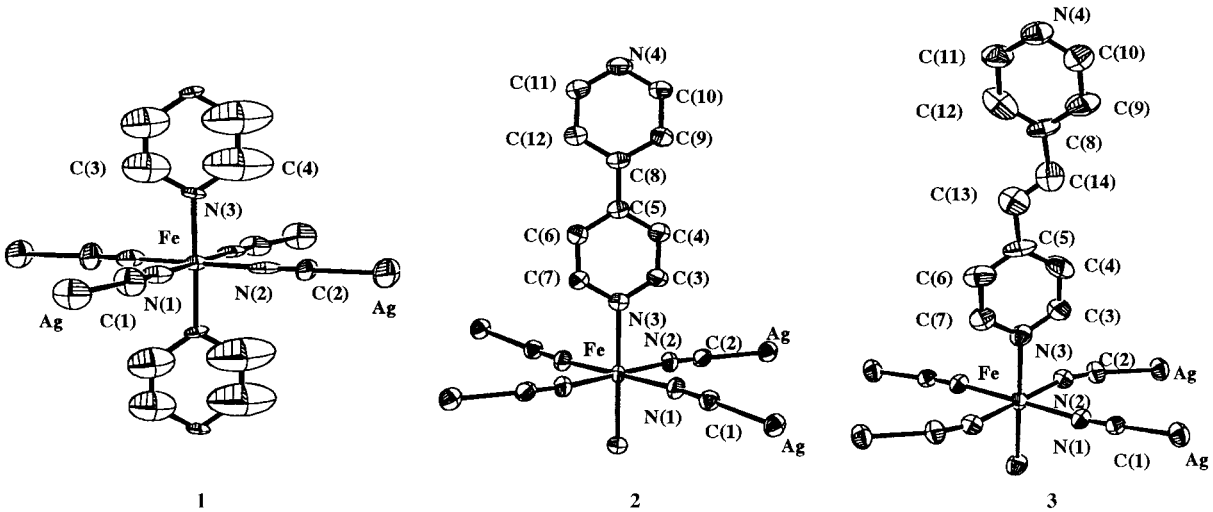

1 **2** **3**

Figure 1. Perspective view of the representative fragments of **1**–**3** including the non-hydrogen atom numbering. Hydrogen atoms are omitted for clarity.

angle. The iron-to-nitrogen bond lengths in the basal plane are Fe–N(1) = 1.91(3) Å and Fe–N(2) = 1.99(3) Å for **1**. The remaining axial positions are occupied by two nitrogen atoms of two pz ligands [Fe–N(3) = 1.98(2) Å]. The small distortion of the octahedral coordination together with the short bond lengths indicate that the iron(II) ion is in the LS singlet ground state; this is confirmed by magnetic susceptibility measurements of **1**. The iron atoms of **2** and **3** are at the inversion centre of a strongly distorted coordination octahedron with significantly larger [Fe–N_6] bond lengths: Fe–N(1) = 2.129(3)/2.129(7) Å, Fe–N(2) = 2.188(3)/2.172(9) Å and Fe–N(3) = 2.248(3)/2.232(7) Å for **2** and **3**, respectively. These values are typical for the iron(II) ion in the HS quintet ground state.

The two interpenetrating nets are displayed in Figure 2. Each $[Ag(CN)_2]^-$ group connects two iron atoms defining the edges of a $\{Fe_4\ [Ag(CN)_2]_4\}$ rhombus. The iron-to-iron distance through the Fe-NC-Ag-CN-Fe edge is 10.242(3) Å (**1**), 10.309(6) Å (**2**) or 10.212(9) Å (**3**), whereas the iron-to-iron separations through the diagonals of the rhombus are 15.98(1) Å and 12.81(1) Å (**1**), 17.03(1) Å and 11.66(1) Å (**2**) and 16.96(1) Å and 11.38(1) Å (**3**). The internal angles are 102.54(1)° and 77.46(1)° (**1**), 111.36(1)° and 68.64(1)° (**2**), and 112.25(1)° and 67.73(1)° (**3**). The edge-shared rhombuses define the grid-layered structure mentioned above, with all the iron and silver atoms in a coplanar sheet (*x*,*y* plane) for **1**. In contrast, the layers are corrugated in **2** and **3** as the C-Ag-C units are bent out of the planes parallel to the direction [010] defined by the iron atoms. The layers alternate in such a way that the iron atom in an adjacent layer is above and below but slightly displaced from the centre, in the case of **1**, and strictly at the centre of the $\{Fe_4\ [Ag(CN)_2]_4\}$ rhombus in **2** and **3**. As mentioned above, one pz ligand and two 4,4′-bipy (**2**) or two bpe (**3**) ligands thread the meshes of the immediately adjacent layers and bind to the iron atom (**1**) or silver atom (**2**, **3**) in a subsequent 2D network defining the two independent interpenetrated 3D networks. In addition, a strongly disordered enclathrated molecule of pz resides in **1**.

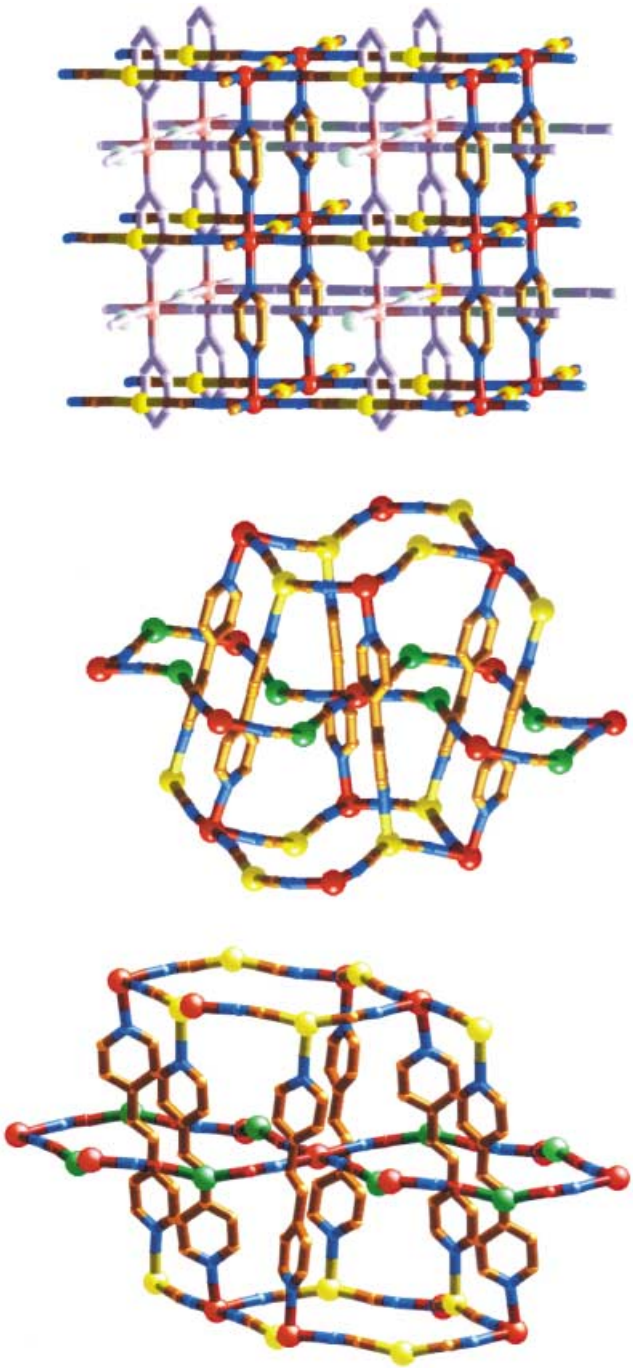

Figure 2. View of the interpenetrating double framework structure of **1** (top), **2** (middle) and **3** (bottom). Fe: red, Ag (subnet-1): yellow, (subnet-2): green, N: blue and C: brown.

Magnetic properties: Compound **1** is in the LS singlet ground state as it is practically diamagnetic at room temperature. However, **2** and **3** are paramagnetic with the $\chi_M T$ product equal to 3.7 (**2**) and 3.6 $cm^3 K mol^{-1}$ (**3**) at 300 K, χ_M being the molar magnetic susceptibility and T the temperature. These values are in the range expected for an iron(II) atom in the HS state. At 1 bar, the $\chi_M T$ value of **2** remains constant as the temperature is lowered from 300 K to 125 K and then decreases smoothly to a value of 2.3 $cm^3 K mol^{-1}$ on cooling down to 5 K. This fact is most likely due to the occurrence of zero-field splitting (ZFS) in the quintet ground; consequently, no spin transition is observed for this compound in the whole range of temperatures (see Figure 4, top).

Figure 3 displays the thermal dependence of $\chi_M T$ for single crystals of **3**. As the temperature is lowered from 300 to 150 K $\chi_M T$ remains constant (3.6 $cm^3 K mol^{-1}$) then decreases abruptly from 150 K down to 95 K. The plateau observed in the region of temperature 90–30 K corresponds to 1.1 $cm^3 K mol^{-1}$. These features reveal an incomplete HS ↔ LS spin conversion. The subsequent dropping of $\chi_M T$ at temperatures below 30 K corresponds to the zero-field splitting of the remainder of HS molecules trapped at low temperatures, about 30 % (see Figure 4, bottom). The warming and cooling modes cause the same magnetic behaviour in the temperature region 5–90 K; however, a hysteresis loop of about 95 K occurs between 120 and 215 K. At 220 K, compound **3** is again in the HS state. It should be emphasised that during the first cooling and warming cycle, a small but significant singularity is observed as the temperature is increased from 90 to 180 K. Firstly, $\chi_M T$ decreases upon warming the sample attaining a value of 0.83 $cm^3 K mol^{-1}$ at

0947-6539/02/0811-2448 $ 20.00+.50/0 *Chem. Eur. J.* **2002**, *8*, No. 11

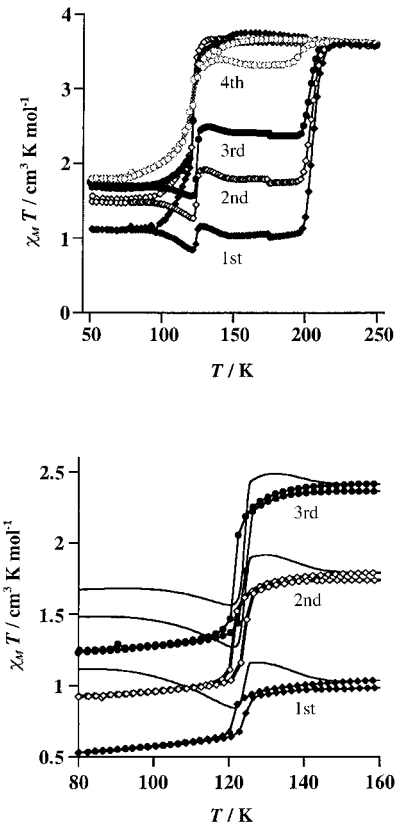

Figure 3. $\chi_M T$ versus T plots for **3**. Top: The effect of warming and cooling cycles on the hysteresis loop. Bottom: Detailed view of the singularity around 120 K and the corresponding cooling and warming cycle in the range 180–80 K.

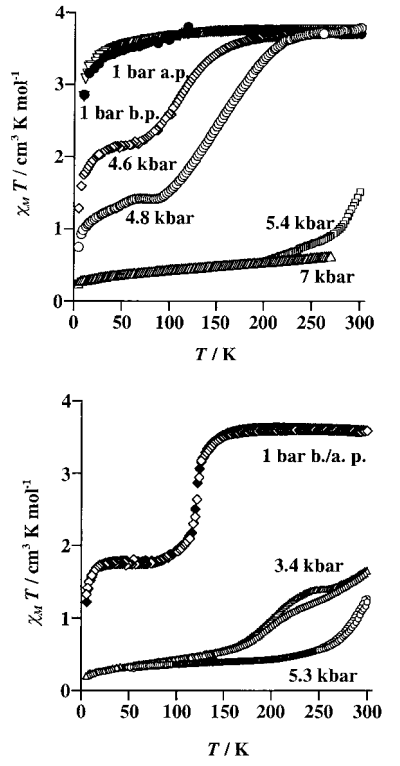

Figure 4. $\chi_M T$ versus T plots for **2** (top) and **3** (bottom) at different pressures.

around 122 K, $\chi_M T$ then increases sharply until it reaches 1.17 cm^3 K mol^{-1} at 126 K, and finally $\chi_M T$ decreases again when the temperature is raised from 126 K to 150 K. Between 150 and 200 K, $\chi_M T$ has a constant value of around 1 cm^3 K mol^{-1}. The sample was cooled from 180 K to 80 K, without leaving the LS phase, in order to check this singularity. Interestingly, around 50% of the trapped HS molecules undergo a secondary spin transition with a small hysteresis 4 K wide. $\chi_M T$ decreases to a value of 0.5 cm^3 K mol^{-1} at 80 K, which corresponds to 14% of still trapped HS molecules (see Figure 3, bottom). This procedure was repeated three more times with the same sample. Each cooling and warming cycle was completed in 11 hours. The main difference after successive cooling and warming cycles is the increase of the trapped HS species at temperatures below 100 K and, hence, the increase of the corresponding $\chi_M T$ values of the low temperature plateau from 1.1 to 1.7 cm^3 K mol^{-1}. Moreover, the singularity is much more marked, whereas the plateau inside the hysteresis loop shifts towards higher values of $\chi_M T$ (1.8, 2.4 and 3.3 cm^3 K mol^{-1} for the 2nd, 3rd and 4th cycles, respectively]. These facts indicate that the HS phase increases at the expense of the LS phase but, interestingly, the width of the hysteresis loop does not change significantly after successive heating and warming cycles. In addition, the single crystals crack and transform into a microcrystalline powder, whose magnetic behaviour corresponds to that of the precipitate version of **3**: 50% spin transition without hysteresis. It should be emphasised that the theoretical X-ray powder diffraction (XRPD) spectrum of the single crystals of **3** is virtually the same as that of the experimental XRPD of the corresponding microcrystalline sample. Crystals coming from different syntheses of **3** have essentially the same behaviour as described above.

Magnetic properties under hydrostatic pressure: The effect of pressure on the thermal variation of $\chi_M T$ was studied for single crystals of **2** and microcrystalline powdered samples of **3**. As stated above, **2** is HS over the whole range of temperatures at ambient pressure (see Figure 4); however, when the pressure is increased to 4.6 kbar, a continuous and incomplete spin transition is observed in the temperature range 225–70 K. $\chi_M T$ decreases from 3.7 cm^3 K mol^{-1} at 300 K to 2.2 cm^3 K mol^{-1} at 70 K, and involves around 40% of spin conversion. The increase of pressure from 4.6 kbar to 4.8 kbar induces a remarkable shift of the spin transition to higher temperatures, which takes place between 230 K and 90 K. The low-temperature plateau ($\chi_M T = 1.4$ cm^3 K mol^{-1}) suggests that around 62% of molecules undergo spin conversion. At 5.4 kbar, a drastic change in magnetic behaviour is observed, the low-spin state dominates at room temperature, $\chi_M T =$ 1.6 cm^3 K mol^{-1}; this value decreases to 0.3 cm^3 K mol^{-1} when the sample is cooled to 5 K. Except for a small residual HS fraction (8%), **2** becomes fully LS at 300 K and 7 kbar ($\chi_M T =$ 0.7 cm^3 K mol^{-1}). After the pressure was released, the $\chi_M T$ against T curves of **2** at 1 bar superimpose quite well; this indicates that no irreversible effects occur under pressure. All the measurements were performed in the cooling and warming modes and no hysteresis was observed. The $\chi_M T$ against T curves for **3** at different pressures are depicted in Figure 4

  0947-6539/02/0811-2449 $ 20.00+.50/0

(bottom). The $\chi_M T$ values at 300 K and pressures of 1 bar, 3.4 kbar and 5.3 kbar are 3.6, 1.7 and 1.3 $cm^3 K mol^{-1}$, respectively. The $\chi_M T$ against T plot at 3.4 kbar for the cooling and warming modes denotes the occurrence of a small hysteresis loop, which is reminiscent of the magnetic properties of the sample constituted of single crystals above described.

The plot of $\chi_M T$ at 300 K versus P for **2** (Figure 5) shows the unusual discontinuous character of the pressure-induced spin transition at room temperature. $\chi_M T$ is constant at 3.7 $cm^3 K mol^{-1}$ up to 4.8 kbar, then decreases dramatically between 4.8 and 7 kbar to 0.7 $cm^3 K mol^{-1}$. This effect is even more dramatic for compound **3**.

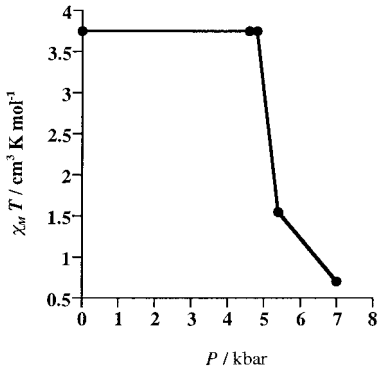

Figure 5. $\chi_M T$ versus P plot at 300 K for **2**.

Photomagnetic behaviour: **LIESST and HS → LS relaxation experiments**: The LIESST experiment was carried out on a microcrystalline (precipitated) sample (0.72 mg) of **3**. The results are displayed in Figure 6. The magnetic response was

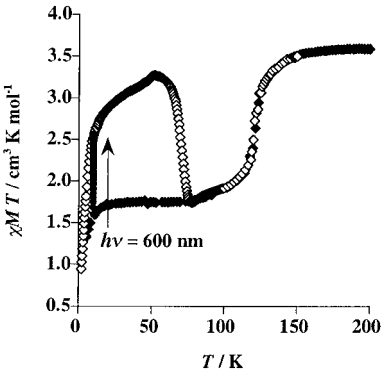

Figure 6. $\chi_M T$ versus T plots for **3**. The sample was cooled from 300 to 5 K at 2 K min^{-1} (◆), then irradiated (600 nm) for 120 min at 10 K (●) and finally warmed from 2 K up to 150 K (0.5 K min^{-1}) after the light irradiation was turned off (◇).

measured first in the cooling mode (cooling rate 2 K min^{-1}) from 300 K down to 10 K with an applied magnetic field of 1.5 T (●). At 10 K, the sample was irradiated with orange light (600 nm) for 120 min, the time required to attain the saturation value of $\chi_M T = 2.6$ $cm^3 K mol^{-1}$ (◆). The light was then switched off, and the temperature was first decreased to 2 K and then increased to 150 K at a rate of 0.5 K min^{-1}. $\chi_M T$ increased progressively up to about 3.3 $cm^3 K mol^{-1}$ at 53 K. Taking into account the occurrence of ZFS in the low temperature region, an almost quantitative LIESST effect has been achieved for **3**. At temperatures greater than 53 K, $\chi_M T$ drops rapidly to reach the minimum value, 1.70 $cm^3 K mol^{-1}$, at 78 K; this indicates the occurrence of HS → LS relaxation. At temperatures greater than 85 K, $\chi_M T$ increases again following the conversion observed on the cooling mode. The characteristic temperature corresponding to the maximum variation of $\chi_M T$ in the HS → LS relaxation after LIESST, $T_{CLIESST}$,[7] is about 71 K.

The dynamics of the HS → LS relaxation was investigated over the temperature range 55–67 K. For higher temperatures, relaxation was too fast relative to the SQUID (superconducting quantum interference device) time window. The decay of the HS molar fraction of the centres that undergo spin conversion, n_{HS}, versus time at various temperatures is displayed in Figure 7. A single-exponential law was used to fit the data according to the expression:

$$n_{HS} = \exp[-k(T)t]$$

in which $k(T)$ corresponds to the relaxation rate at temperature T. The parameter $k(T)$ was determined by a least-squares fit minimising $R = \Sigma[(n_{HS})_{obsd} - (n_{HS})_{calcd}]^2 / \Sigma[(n_{HS})_{obsd}]^2$. The best fits are shown in Table 3, and the resulting least-squares curves are shown as solid lines in Figure 7.

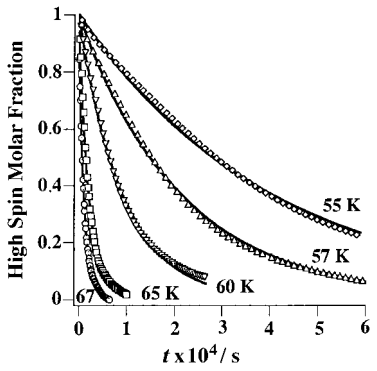

Figure 7. Selected time dependence at various temperatures of the HS molar fraction of the active centres, n_{HS}, generated by the LIESST effect. Solid line represents the best fit to the experimental HS → LS relaxation curves.

Table 3. Best fit of $k(T)$ for the HS → LS relaxation of **3** over the temperature range 55–67 K.

$k(T)$ [s^{-1}]	R	T [K]
2.5×10^{-5}	4×10^{-4}	55
4.6×10^{-5}	5×10^{-4}	57
1.1×10^{-4}	8×10^{-4}	60
4.5×10^{-5}	1×10^{-3}	65
6.1×10^{-4}	9×10^{-4}	66
8.1×10^{-4}	8×10^{-4}	67

Conclusion

Cooperativity is responsible for the dramatic changes observed in the magnetic and optical properties of spin-crossover compounds. It strongly depends on the effectiveness of

0947-6539/02/0811-2450 $ 20.00+.50/0 *Chem. Eur. J.* **2002**, *8*, No. 11

the intermolecular contacts in the crystal. Strong intermolecular interactions result from the presence of an efficient hydrogen-bonding network or π staking between the building blocks used for the construction of the spin-crossover compound. While the supramolecular synthesis from mononuclear units is a complex task, which is far from being accomplished, the synthesis of polymeric spin crossover compounds represents an interesting alternative for exploring cooperativity. In this regard, a number of one-, two- and three-dimensional compounds have been reported. For instance, the compounds $[Fe(4\text{-R-trz})_3](anion)_2 \cdot x\,H_2O$ (4-R-trz = 4-substituted 1,2,4-triazole)[8] and $[Fe(btzp)_3](ClO_4)_2$ (btzp = 1,2-bis-(tetrazole-1-yl)propane)[9] are the most representative 1D spin crossover compounds studied up to now. The former system defines a family of compounds displaying strong cooperativity with large hysteresis loops, whereas a less cooperative and continuous spin conversion is observed for the BTZP derivative. The rigidity of the triazole iron-bridged chain and the flexibility of the unsaturated linkages connecting the two tetrazole moieties are at the heart of the different cooperativity observed in these 1D compounds.

Sharp spin changes with thermal hysteresis have also been reported for the 2D system $[Fe(btr)_2(NCX)_2] \cdot H_2O$ (btr = 4,4′-bis-1,2,4-triazole; X = S[10] and Se[11]) and for the compound $[Fe\{N(entz)_3\}_2](anion)_2$ (N(entz) = tris[(tetrazole-1-yl)ethane]amine; anion = BF_4^-, and ClO_4^-).[12] Only two 3D coordination spin-crossover polymers based either on triazole or tetrazole derivatives have been reported up to now. They are $[Fe(btr)_3](ClO_4)_2$[13] and $[Fe(btzb)_3](ClO_4)_2$ (btzb = 1,4-bis-(tetrazole-1-yl)butane).[14]

We have investigated the suitability of the bismonodentate ligands pz, bpe and bpb (bpb = 1,4-bis(4-pyridyl)-butadyine) for the synthesis of new 2D polymers of formula $[Fe(L)_2(NCS)_2]n$S. No spin transition has been observed, even at 10 kbar, for the 2D antiferromagnet $[Fe(pz)_2(NCS)_2]$.[15] In contrast, a thermal continuous and incomplete spin conversion was observed for the bpe (nS = 1 MeOH)[16] and bpb (nS = 0.5 MeOH)[17] derivatives at 1 bar. The structural motive is similar for the three compounds: the equatorial positions of the $[FeN_6]$ core being occupied by nitrogen atoms of the bis-monodentate ligands, while the remaining two positions are filled by the thiocyanate anions. From the structural point of view this series represents an interesting correlation between the size of the ligand and the degree of catenation in (4,4) 2D systems. The pz derivative shows no interpenetration of the 2D nets, while bpe and bpb derivatives show double and triply interlocked 2D nets, respectively.

The 2D and 3D Hofmann-like spin crossover polymers of formula $\{Fe(L)_x[M^{II}(CN)_4]\}n$G with L = pyridine ($x = 2$, $n = 0$); pz ($x = 1$, nG = 2 H_2O) and M^{II} = Ni, Pd, Pt represent a qualitative and quantitative improvement in the search for new polymeric spin-crossover materials.[5] In these compounds, polymerisation takes place through the rigid $[M^{II}(CN)_4]^{2-}$ moieties, which occupy the four equatorial positions of the $[FeN_6]$ core and the two axial positions are occupied by the nitrogen atom of the organic ligand. In the case of the pz derivatives, polymerisation also takes place via the bis-monodentate pz ligand giving the 3D network. In the present paper we have extended this approach to the $[Ag(CN)_2]^-$ anion using pz, 4,4′-bipy and bpe as bridging ligands. It should be pointed out that **1** presents an infinite 2D network defined by edge-shared $\{Fe_4[Ag(CN)_2]_4\}$ rhombuses, and that these sheets are interconnected by the pz ligand in such a way that interpenetration of two 3D identical subnets takes place. By contrast, no interpenetration is observed for the $\{Fe(pz)[M^{II}(CN)_4]\} \cdot 2H_2O$ compounds as the voids defined by the tetradentate ligand $[M^{II}(CN)_4]^{2-}$ are four times smaller than those corresponding to the $[M^{I}(CN)_2]^-$ anions. Interestingly, the bond length Fe–N(pz) = 2.267(4) Å observed for $\{Fe(pz)[Pt(CN)_4]\} \cdot 2H_2O$ is significantly larger than that of **1** [Fe–N(3) = 1.98(2) Å]. This fact reflects the different ground state of these compounds as they are HS and LS at room temperature, respectively. From these results an average variation of the metal-to-ligand bond length of around 0.29 Å could be anticipated for these polymeric compounds upon spin conversion. This large structural modification could account for the strong cooperative behaviour observed for all the cyanide compounds studied up to now.

Interpenetration takes place in a different way for **2** and **3**. The axial positions of each iron atom are occupied by two organic bridging ligands but, at variance with **1**, these ligands link two Ag atoms belonging to alternate $\{Fe_4[Ag(CN)_2]_4\}_n$ sheets so that each $\{Fe_4[Ag(CN)_2]_4\}$ window of contiguous sheets is threaded twice by the organic bridges. Compound **3** shows one of the largest thermal hystereses (ca. 95 K wide) observed for a spin-crossover compound. However, the single crystals crack with concomitant loss of hysteresis after repeated cycles of cooling and heating. This loss of "memory" is uncommon because the HS fraction increases without essential narrowing of the hysteresis loop. After five or more cooling and warming cycles, the single crystals are completely destroyed, and the magnetic behaviour becomes similar to that of the precipitated microcrystalline samples of **3**, showing a 50 % spin transition. This indicates that irreversible changes occur in the solid state and strongly suggests that only one subnet undergoes thermal spin conversion at 1 bar. Nevertheless, such changes do not involve crystallographic phase transition. There are some well documented iron(II) spin-crossover compounds for which incomplete spin conversion at low temperature has been observed. Usually, small differences are observed in the Fe–N bond lengths for the two different iron atoms in these compounds, see for instance ref. [17] and references therein.

Pressure usually causes a tendency towards the closer packing of molecules. This increases the intermolecular interactions and makes the metal-to-ligand bond lengths shorter. So, the general effect of pressure on transition metal complexes in the solid state is to increase the ligand field and reduce the interelectronic repulsion.[18, 19] When the ligand field of the iron(II) is close to the crossing point, these changes can result in a HS → LS conversion at relatively low pressures.[20, 21] In this regard, the crystal structures of **2** and **3** are very similar, the average Fe–N bond length is only 0.011(9) Å greater for **2**; however, despite this small difference, **2** is HS while **3** (single-crystal form) undergoes thermal spin transition at 1 bar, which shows a large thermal hysteresis. By

contrast, the thermal spin conversion induced under pressure for **2** takes place without thermal hysteresis, being similar to that observed for **3** in the microcrystalline form. It is important to point out that more than 85% of the spin transition takes place within the range of 2 kbar at room temperature. Though no hysteresis is observed, the extreme sensitivity of **2** and **3** to pressure at 300 K suggests the occurrence of strong cooperativity in the 3D network.

The discovery of the LIESST effect[22] in the solid state created the expectation that the spin crossover compounds could be used as optical switches. Unfortunately, the long-lived meta-stable HS state only is achieved at temperatures lower than 50 K for most compounds. However, it has been suggested that the creation of a long-lived meta-stable HS state after the LIESST effect could be achieved by increasing cooperativity, as this magnifies the activation-energy barrier between the LS and HS potential wells.[23] The photomagnetic studies of **3** are the first example of LIESST effect observed for a 3D polymeric compound. In our polymeric approach, the iron atoms were connected with rigid rods in order to transmit the intramolecular changes efficiently upon spin conversion, consequently, **3** experiences strong cooperativity. In spite of this fact, the HS $\rightarrow$ LS thermal relaxations are single exponentials instead of sigmoidal curves. Anyway, relaxation curves indicate that a tunnelling mechanism dominates at temperatures as high as 50 K. Consequently, the rate constants $k_{HL}(T)$ are small, and the relaxation process is very slow. However, the relaxation accelerates as the temperature approaches $T_{CLIESST} = 71$ K indicating that thermal activation becomes the predominant mechanism. It is important to note that the lowest $\chi_M T$ value attained in the relaxation experiments, after long delays, is 1.6 $cm^3 K mol^{-1}$. This indicates that the 50% plateau does not corresponds to a meta-stable trapped HS state as observed previously for the compound $\{Fe(abpt)_2[N(CN)_2]_2\}$.[24]

Experimental Section

Materials: Pyrazine, 4,4′-bipyridine, bispyridyl-ethylene, $K[Ag(CN)_2]$ and $Fe(BF_4)_2 \cdot 6H_2O$ were purchased from commercial sources and used as received.

Preparation of 1, 2 and 3: Samples of **1**, **2** and **3** were obtained as crystalline materials by the slow diffusion method in water/methanol and under an argon atmosphere, with H-double-tube glass vessels. The starting materials were an aqueous solution of $K[Ag(CN)_2]$ (3 mL, 0.54 mmol) on one hand and a methanolic solution of $Fe(BF_4)_2 \cdot 6H_2O$ and L (1:1, 5 mL, 0.27 mmol) on the other. After 2–4 weeks, deep red single crystals of **1**, **2** and **3** were collected, washed in water/methanol (1:1) and dried in an argon stream. Yields: 12% (**1**), 6% (**2**) and 5% (**3**). Elemental analysis calcd (%) for $C_{12}H_8N_8Ag_2Fe$ (535.85) (**1**): C 26.87, H 1.49, N 20.90; found: C 26.8, H 1.6, N 20.6; for $C_{24}H_{16}N_8Ag_2Fe$ (344.02) (**2**): C 41.86, H 2.32, N 16.28; found: C 41.7, H 2.3, N 16.1; for $C_{28}H_{20}N_8Ag_2Fe$ (740.11) (**3**): C 45.40, H 2.70, N 15.13; found: C 45.2, H 2.7, N 14.9.

Magnetic and photomagnetic measurements: The variable-temperature magnetic susceptibility measurements were carried out on small single crystal (20–30 mg) samples by using a Quantum Design MPMS2 SQUID susceptometer equipped with a 5.5 T magnet and operating at 1 T and 1.8–300 K. The magnetic measurements under pressure were performed by using a hydrostatic pressure cell, specially designed for our SQUID set up, made of hardened beryllium bronze with silicon oil as the pressure transmitting medium and operating over the pressure range 1 bar–12 kbar. The cylindrically shaped sample holder was 1 mm in diameter and 5–7 mm in length. The pressure was measured by using the pressure dependence of the superconducting transition temperature of a built-in pressure sensor made of high-purity tin.[25] The susceptometer was calibrated with $(NH_4)_2Mn(SO_4)_2 \cdot 12H_2O$. Photomagnetic experiments were carried out by using a Xe lamp with a 600 nm filter coupled through an optical fibre to the SQUID susceptometer; the out power was 2 $mW cm^{-2}$. Experimental susceptibilities were corrected for diamagnetism of the constituent atoms by the use of Pascal's constants.

X-ray crystallography: Diffraction data on prismatic crystals of **1**–**3** were collected at 293 K with a Siemens P-4 diffractometer by using graphite-monochromated $Mo_{K\alpha}$ radiation ($\lambda = 0.71073$ Å) and the $\theta-2\theta$ scan technique. The cell parameters were determined from least-squares refinement of 25 well-centred reflections in the range $12 < \theta < 20°$. The crystal parameters and refinement data are summarised in Table 1. Three standard reflections were monitored every hour, but no intensity variations were observed. Lorentz polarisation and absorption corrections were applied to the data. The structures were solved by direct methods using SHELXS97 and refined the full-matrix least-squares method on F^2 using SHELXL97.[26] All non-hydrogen atoms were refined anisotropically.

CCDC-174175 (**1**), 174176 (**2**), and 174177 (**3**) contain the supplementary crystallographic data for this paper. These data can be obtained free of charge via www.ccdc.cam.ac.uk/conts/retrieving.html (or from the Cambridge Crystallographic Data Centre, 12 Union Road, Cambridge CB2 1EZ, UK; fax: (+44) 1223-336033; or deposit@ccdc.cam.uk.

Acknowledgement

We are grateful for financial support from the European Commission, granting the TMR-Network "Thermal and Optical Switching of Spin States (TOSS)", Contract No. ERB-FMRX-CT98–0199EEC/TMR. We thank the Spanish DGICYT for financial assistance through Project PB97–1397.

[1] O. Kahn, C. J. Martinez, *Science* **1998**, *279*, 44.
[2] P. Gutlich, A. Hauser, H. Spiering, *Angew. Chem.* **1994**, *106*, 2109; *Angew. Chem. Int. Ed. Engl.* **1994**, *33*, 2024.
[3] E. König, *Prog. Inorg. Chem.* **1987**, *35*, 527.
[4] T. Kitazawa, Y. Gomi, M. Takahashi, M. Takeda, M. Enomoto, A. Miyazaki, T. Enoki, *J. Mater. Chem.* **1996**, *6*, 119.
[5] V. Niel, J. M. Martínez-Agudo, M. C. Muñoz, A. B. Gaspar, J. A. Real, *Inorg. Chem.* **2001**, *40*, 3838.
[6] a) T. Iwamoto in *Inclusion Compounds*, *Vol. 5* (Eds.: J. L. Atwood, J. E. D. Davies, D. D. MacNicol), Oxford University Press, Oxford, **1991**, p. 177; b) T. Iwamoto in *Chemistry of Microporous Crystals* (Eds.: T. Inui, S. Namba, T. Tatsumi), Kodansha/Elsevier, Tokyo, **1991**, p. 1; c) T. Soma, H. Yuge, T. Iwamoto, *Angew. Chem.* **1994**, *106*, 1746; *Angew. Chem. Int. Ed. Engl.* **1994**, *33*, 1665.
[7] J. F. Létard, L. Capes, G. Chastanet, N. Moliner, S. Létard, J. A. Real, O. Kahn, *Chem. Phys. Lett.* **1999**, *313*, 115.
[8] a) L. G. Lavrenova, V. N. Ikorskii, V. A. Varmek, I. M. Oglezneva, S. V. Larionov, *Koord. Khim.* **1986**, *12*, 207; b) L. G. Lavrenova, V. N. Ikorskii, V. A. Varmek, I. M. Oglezneva, S. V. Larionov, *Koord. Khim.* **1990**, *16*, 654; c) L. G. Lavrenova, N. G. Yudina, V. N. Ikorskii, V. A. Varmek, I. M. Oglezneva, S. V. Larionov, *Koord. Khim.* **1995**, *14*, 1333; d) Y. Garcia, P. J. van Koningsbruggen, E. Codjovi, R. Lapouyade, O. Kahn, L. Rabardel, *J. Mater. Chem.* **1997**, *7*, 857; e) Y. Garcia, P. J. van Koningsbruggen, R. Lapouyade, L. Fournès, L. Rabardel, O. Kahn, V. Ksenofontov, G. Levchenko, P. Gütlich, *Chem. Mater.* **1998**, *10*, 2426; f) P. J. van Koningsbruggen, Y. Garcia, E. Codjovi, R. Lapouyade, O. Kahn, L. Fournès, L. Rabardel, *J. Mater. Chem.* **1997**, *7*, 2069.
[9] P. J. van Koningsbruggen, Y. Garcia, O. Kahn, L. Fournès, H. Kooijman, A. L. Spek, J. G. Haasnoot, J. Moscovici, K. Provost, A. Michalowicz, F. Renz, P. Gütlich, *Inorg. Chem.* **2000**, *39*, 1891.
[10] W. Vreugdenhil, J. H. van Diemen, R. A. G. de Graaff, J. G. Haasnoot, J. Reedijk, A. M. van der Kraan, O. Kahn, J. Zarembowitch, *Polyhedron* **1990**, *9*, 2971.
[11] A. Ozarowski, Y. Shunzhong, B. R. McGarvey, A. Mislankar, J. E. Drake, *Inorg. Chem.* **1991**, *30*, 3167.

  0947-6539/02/0811-2452 $ 20.00+.50/0 *Chem. Eur. J.* **2002**, *8*, No. 11

[12] R. Bronisz, Z. Ciunik, K. Drabent, M. F. Rudolf *Conference Proceedings*, *ICAME-95* **1996**, *50*, 15.
[13] Y. Garcia, O. Kahn, L. Rabardel, B. Chansou, L. Salmon, J. P. Tuchagues, *Inorg. Chem.* **1999**, *38*, 4663.
[14] P. J. van Koningsbruggen, Y. Garcia, H. Kooijman, A. L. Spek, J. G. Haasnoot, O. Kahn, J. Linares, E. Codjovi, F. Varret, *J. Chem. Soc. Dalton Trans.* **2001**, 466.
[15] J. A. Real, G. De Munno, M. C. Muñoz, M. Julve, *Inorg. Chem.* **1991**, *30*, 2701.
[16] J. A. Real, E Andrés, M. C. Muñoz, M. Julve, T. Granier, A. Bousseksou, F. Varret, *Science* **1995**, *268*, 265.
[17] N. Moliner, M. C. Muñoz, S. Létard, X. Solans, N. Menéndez, A. Goujon, F. Varret, J. A. Real, *Inorg. Chem.* **2000**, *39*, 5390.
[18] H. G. Drickamer, *Solid State Physics.* **1965**, *17*, 1.
[19] D. R. Stephens, H. G. Drickamer, *J. Chem. Phys.* **1961**, *35*, 427.
[20] H. G. Drickamer, *Int. Rev. Phys. Chem.* **1982**, *2*, 171.
[21] H. G. Drickamer, C. V. Franck, *Electronic Transitions and the High Pressure Chemistry and Physics of Solids*, Chapman and Hall: London, **1973**.
[22] S. Decurtins, P. Gutlich, C. P. Köhler, H. Spiering, A. Hauser, *Chem. Phys. Lett.* **1984**, *105*, 1.
[23] a) A. Desaix, O. Roubeau, J. Jeftic, J. G. Haasnoot, K. Boukheddaden, E. Codjovi, J. Linares, M. Nogués, F. Varret, *Eur. Phys. J. B* **1998**, *6*, 183; b) F. Varret, K. Boukheddaden, J. Jeftic, O. Roubeau, *Mol. Cryst. Liq. Cryst.* **1999**, *335*, 1273.
[24] N. Moliner, A. B. Gaspar, M. C. Muñoz, V. Niel, J. Cano, J. A. Real, *Inorg. Chem.* **2001**, *40*, 3986.
[25] a) V. P. Dyakonov, G. G. Levchenko, *Sov. J. Pribori Texnika Eksperimenta* **1983**, *5*, 236; b) M. Baran, G. G. Levchenko, V. P. Dyakonov, G. Shymchak, *Physica C* **1995**, *241*, 383.
[26] G. M. Sheldrick, SHELX97, *Program for Crystal Structure Determination*, University of Gottingen, Germany, **1997**.

Received: November 23, 2001 [F3702]